Calorimetry can detect the early onset of hydrolysis in hybrid supercapacitors with aqueous electrolytes

Matevž Frajnkovič [a], Ampol Likitchatchawankun [b], Camille Douard [c,d], Yucheng Zhou [a], Sun Woong Baek [a], Ivan Catton [a], Olivier Crosnier [c,d], Thierry Brousse [c,d], Laurent Pilon [a,e,*]

[a] Mechanical and Aerospace Engineering Department, Henry Samueli School of Engineering and Applied Science, University of California, Los Angeles, CA 90095, USA
[b] Mechanical Engineering Simulation and Design Group, The Sirindhorn International Thai-German Graduate School of Engineering (TGGS), King Mongkut's University of Technology North Bangkok (KMUTNB), 1518 Parcharat 1 Road, Wongsawang, Bangsue, Bangkok 10800, Thailand
[c] Nantes Université, CNRS, Institut des Matériaux de Nantes Jean Rouxel, IMN, F-44000 Nantes, France
[d] Réseau sur le Stockage Electrochimique de l'Energie (RS2E), CNRS, FR 3459 33 rue Saint Leu, 80039 Amiens Cedex, France
[e] California NanoSystems Institute, University of California, Los Angeles, CA 90095, USA

HIGHLIGHTS

- Heat generation measured in α-MnO$_2$ and AC electrodes in aqueous electrolytes.
- Endothermic signature of hydrolysis was measured at α-MnO$_2$ electrodes above 1.6 V.
- Hydrolysis was delayed in aqueous electrolytes with thinner cation solvation shell.
- Calorimetry could detect the onset of hydrolysis before electrochemical techniques.
- Heat generation at AC electrodes was due to EDL formation and ion desolvation.

GRAPHICAL ABSTRACT

ARTICLE INFO
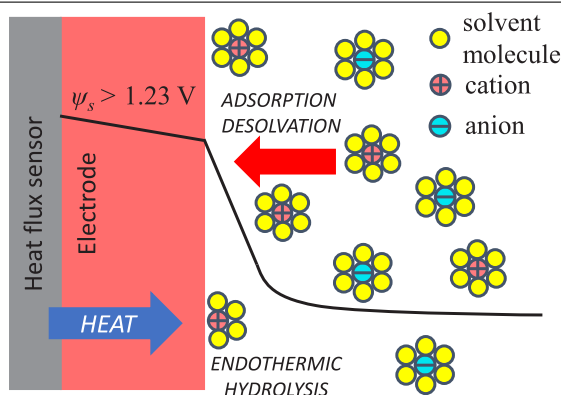
ABSTRACT

This study investigates the effect of cation species on the onset of electrolyte hydrolysis in hybrid supercapacitors with aqueous electrolytes using isothermal operando calorimetry. The cells consisted of a positive α-MnO$_2$ cryptomelane electrode and a negative activated carbon (AC) electrode with either 0.5 M K$_2$SO$_4$ or 0.5 M Cs$_2$SO$_4$ aqueous electrolytes. They were characterized using cyclic voltammetry and galvanostatic cycling. In addition, the instantaneous heat generation rate at each electrode was measured using a custom isothermal operando calorimeter. Heat generation associated with resistive losses (Joule heating) and reversible ion adsorption/desorption was clearly identified. For larger potential windows, an endothermic dip, attributed to the onset of hydrolysis, was observed at the positive α-MnO$_2$ electrode where K$^+$ and Cs$^+$ ions engaged in fast surface redox reactions. Interestingly, this endothermic dip appeared at 1.8 V and 2.0 V for K$_2$SO$_4$ and Cs$_2$SO$_4$ aqueous electrolytes, respectively. The difference in the stable operating potential window was attributed to thinner solvation shell around Cs$^+$ cation than for K$^+$ thus reducing the amount of water present near the electrodes as ions partially shed their solvation shells during adsorption. The early onset of hydrolysis could be observed by isothermal operando calorimetry before it could be observed with conventional electrochemical methods.

---

* Corresponding author at: Mechanical and Aerospace Engineering Department, Henry Samueli School of Engineering and Applied Science, University of California, Los Angeles, CA 90095, USA.
E-mail address: pilon@seas.ucla.edu (L. Pilon).

Nomenclature

a	Effective ion diameter (nm)
A	Footprint area of the heat flux sensor (cm^2)
C	Capacity (mAh)
C_g	Gravimetric capacity (mAh g^{-1})
D	Diffusion coefficient (m^2 s^{-1})
H_{sol}	Hydration molar enthalpy (kJ mol^{-1})
I	Electric current (mA)
j	Cycle number (–)
m	Mass loading of active material in electrode (mg)
q''	Heat flux (mW cm^{-2})
$\dot{Q}$	Heat generation rate (mW)
R_s	Internal resistance for the entire device (Ω)
S	Heat flux sensor sensitivity (μV $(W/cm^2)^{-1}$)
t	Time (s)
t_c^-	Time immediately after the beginning of the discharging step (s)
t_c^+	Time at the end of the charging step (s)
T	Temperature or absolute temperature (°C or K)
ΔV	Voltage difference generated in the heat flux sensor (μV)
z_i	Valency (–)

Greek symbols

|	
ν	Scan rate (mV s^{-1})
σ	Ionic conductivity (mS cm^{-1})
ψ_{EW}	Electrolysis potential of water (V)
$\psi_{s,min}, \psi_{s,max}$	Minimum, maximum cell potential (V)
$\psi_s(t)$	Cell potential (V)

Superscripts and subscripts

AC	Refers to activated carbon electrode
$-$	Refers to unsolvated anions
$-,s$	Refers to solvated anions
c	Refers to charging step
$+$	Refers to unsolvated cations
$+,s$	Refers to solvated cations
d	Refers to discharging step
i	Refers to electrode i
MnO_2	Refers to cryptomelane electrode

1. Introduction

Hybrid or asymmetric supercapacitors bridge the gap between conventional batteries and electrical double layer capacitors (EDLCs) [1–3]. Batteries exhibit high energy densities as they store electrical energy via redox reactions [4–6]. However, their power density and cycle life is often limited by the relatively slow ion intercalation (i.e., Li^+, Na^+) in the electrode material, and sometimes, the slow phase transition taking place upon insertion/deinsertion of metal ions during operation [7,8]. By contrast, EDLCs have high power density as they store electrical charge physically by ion adsorption over the large surface area of mesoporous carbon electrodes [9–13]. However, EDLCs exhibit much smaller energy density than batteries [7,8]. On the other hand, hybrid supercapacitors consist of a pseudocapacitive transition metal oxide electrode [14] and an activated carbon counter electrode [15–17]. They store electrical energy via both ion adsorption/desorption

and fast reversible redox reactions without inducing phase transition. These attributes enable them to achieve high power densities while maintaining reasonable energy densities [18–20]. Alternatively, asymmetric supercapacitors, involving a battery-type electrode as one of the electrodes and an activated carbon electrode as the complementary electrode such as in lithium-ion capacitors, have also been proposed. They feature even larger energy density, lower power density and have limited cycle life [21,22]. Despite this last remark, the wording hybrid or asymmetric supercapacitor has been equally used in the past to designate either (i) a device involving a battery-type electrode or (ii) a device with a pseudocapacitive electrode. In both cases, such electrodes are coupled with a capacitive activated carbon electrode. In what follows, hybrid supercapacitor refers to the cells investigated in the present manuscript.

Various transition metal oxides have been considered as pseudocapacitive electrode materials due to their large theoretical capacity, high redox reaction reversibility, and chemical stability including MnO_2, MoO_2, Nb_2O_5, V_2O_5, and Fe_3O_4, to name a few [23,24]. Two different charging mechanisms have been proposed for pseudocapacitive electrodes, namely (i) charging through surface or near-surface redox reactions, such as in α-MnO_2 cryptomelane [25–30] and (ii) charging by fast ion intercalation/deintercalation into the channels or layers of the redox-active material without inducing a phase transition, such as in Nb_2O_5 [19,31]. In both cases, the reversible redox reaction can be written as [32],

$$[M_xO_y] + zC^+ + ze^- \underset{\text{charging}}{\overset{\text{discharging}}{\rightleftharpoons}} [(C_z^+)M_xO_{y-z}^-] \quad (1)$$
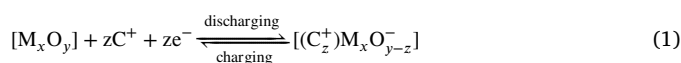
where C^+ refers to alkali metal cations such as K^+ in aqueous electrolytes. Charging via fast surface redox reactions results in nearly rectangular cyclic voltammograms and almost linear temporal evolution of potential under galvanostatic cycling, similar to those obtained with EDLCs [19]. On the other hand, charging via ion intercalation/deintercalation typically results in larger current sometimes featuring redox peaks in cyclic voltammograms and non-linear potential temporal evolution under galvanostatic cycling [19].

Operating batteries, EDLCs, and hybrid supercapacitors under larger potential windows can increase their energy density [15–17,33–35]. However, their operating potential window is limited by the electrochemical stability of the electrolyte. Aqueous electrolytes are inexpensive, non-flammable, non-toxic, and can have a pH close to neutral thus mitigating the risks of corroding the electrodes and current collectors. However, DI water undergoes electrolysis at the potential of 1.23 V at 20 °C and pH of 7, when H_2 and O_2 evolution reactions occur [36]. The electrochemical stability window of aqueous electrolytes can be expanded by keeping the pH of the electrolyte close to neutral by decreasing the concentration of H^+ and OH^- ions in the electrolyte [33]. The mass ratio between the positive and the negative electrodes can also be optimized to ensure the optimal split of the cell potential between the electrodes. As a result, each electrode operates at the highest possible potential without inducing H_2 or O_2 evolution reactions from acidic (H^+) or basic (OH^-) functional groups, respectively [34].

In addition, hybrid supercapacitors with MnO_2/AC electrodes in aqueous electrolytes with (a) 2 M KNO_3 and pH of either 6.4 or 10 [33], (b) 0.5 M Na_2SO_4 and pH of 6.4 [34], (c) 0.65 M K_2SO_4 and pH of 6.5 [16], and (d) 1 M HCl, 1 M KOH, and 1 M KCl (pH not reported) [15] have been shown to operate above the theoretical electrochemical stability window of water of 1.23 V at 20 °C and pH of 7 [15,16,33,34]. This expanded potential window was attributed to the high oxygen evolution overpotential at the MnO_2 electrode and to the low hydrogen evolution overpotential at the AC electrode [16]. Finally, the use of water in salt electrolytes (WISE) with large ion concentrations (≥ 20 M) can also limit the amount of water available to undergo hydrolysis and increase the operating potential window [35,37].

Recently, isothermal *operando* calorimetry measuring the time-dependent heat generation rates, at each electrode separately,

during galvanostatic cycling has been successfully used to identify the thermal signature of different charging mechanisms in EDLCs with aqueous [38], organic [38–41], and ionic liquid [40–42] electrolytes. These mechanisms included (i) ion desolvation and adsorption [39–42], (ii) overscreening effect [39,40], (iii) organic solvent decomposition [42], and (iv) irreversible ion intercalation in AC electrode under different temperatures and potential windows [42]. Moreover, a new in situ cell was developed for simultaneous thermal analysis (STA) to measure simultaneously heat dissipation and weight changes as well as resistance and capacitance in an EDLC device during cycling or float tests [43]. However, few *operando* calorimetry studies have used calorimetry to investigate hybrid supercapacitors [32,44].

The present study aims to use isothermal *operando* calorimetry to investigate the effect of ion species on the maximum operating potential window of α-MnO$_2$ cryptomelane/ activated carbon (AC) hybrid supercapacitors with aqueous electrolytes. Indeed, calorimetry has demonstrated its ability to detect the decomposition of organic solvent in EDLCs under high cell potential and/or high temperature [42]. Here, two different aqueous electrolytes with very different ion sizes and solvation shell thickness, with nearly neutral pH, were considered.

2. Background

2.1. Polymorphs of MnO$_2$

Crystalline manganese dioxide (MnO$_2$) is a naturally abundant mineral that is formed by MnO$_6$ octahedra sharing vertices and edges in various combinations resulting in one, two, or three-dimensional tunnel structures [24,45,46]. Their differences may be characterized by the size (n × m) and number of tunnels as well as the geometry of the tunnels (i.e., 1D, 2D, or 3D) in the MnO$_2$ unit cell [47]. Some MnO$_2$ polymorphs with small 1D tunnels such as pyrolusite (β-MnO$_2$) and nsutite (γ-MnO$_2$) are more likely to exhibit fast surface redox charging mechanism. Then, their capacity is proportional to their surface area, like in EDLCs [24]. By contrast, birnessite (δ-MnO$_2$) forms a 2D lamellar structure and exhibits larger capacity than β- and γ-MnO$_2$, due to cation intercalation/deintercalation [24,48]. In contrast to birnessite, cryptomelane (α-MnO$_2$) features surface redox reactions despite having relatively large tunnels that could facilitate cation intercalation. This can be attributed to the sieve-like structure of α-MnO$_2$ tunnels [48]. Interestingly, both charging mechanisms may take place in other MnO$_2$ polymorphs [24,45,46]. Finally, during cycling of MnO$_2$ electrodes in mild aqueous electrolytes, Mn changes its oxidation state from Mn^{4+} to Mn^{3+} (with eventually dismutation of Mn^{3+} into Mn^{2+} and Mn^{4+}) when discharged with monovalent or bivalent cations, respectively [24, 45,46].

2.2. Onset of hydrolysis

Hong et al. [15] investigated the influence of pH on the potential window limitations of aqueous electrolyte for amorphous MnO$_2$/AC electrodes in 1 M HCl (acidic), 1 M KOH (basic), and 1 M KCl (neutral) aqueous electrolytes. In a three-electrode setup with a Pt metal plate as the reference electrode, the authors observed that in acidic pH, the following H$_2$ evolution reaction began at the AC electrode at −0.2 V when the potential at the MnO$_2$ electrode was 1.0 V both vs. the Pt reference electrode,

$$2H_3O^+ + 2e^- \longrightarrow H_2(g) + 2H_2O. \tag{2}$$

This reaction limited the operating potential window to 1.2 V (< 1.23 V) in 1 M HCl aqueous electrolyte [15]. Similarly in basic pH, the following O$_2$ evolution reaction started at the MnO$_2$ electrode at 0.7 V when the potential at the AC electrode was −1.1 V both vs. the Pt reference electrode,

$$4OH^- \longrightarrow O_2(g) + 2H_2O + 4e^-. \tag{3}$$

Here, the potential window was limited to 1.8 V in 1 M KOH aqueous electrolyte [15]. Moreover, in neutral pH, the H$_2$ and O$_2$ evolution reactions were negligible and the following H$_2$O decomposition reactions were observed for potential window of 2.0 V such that the MnO$_2$ electrode was at 1.1 V and the AC electrode at −0.9 V both vs. the Pt reference electrode [15],

$$2H_2O \longrightarrow O_2(g) + 4H^+ + 4e^-, \tag{4}$$

$$2H_2O + 2e^- \longrightarrow H_2(g) + 2OH^-. \tag{5}$$

Overall, in amorphous MnO$_2$/AC systems with aqueous electrolytes, hydrolysis was delayed in basic and neutral electrolytes with cell potential window exceeding 1.23 V while acidic environment acted as a catalyst for hydrolysis and reduced the maximum cell potential window [15].

2.3. Operando calorimetry

Dandeville et al. [44] developed an *operando* calorimeter equipped with thermocouples for measuring the instantaneous temperature profile of (i) an EDLC cell consisting of two identical AC electrodes and of (ii) a hybrid supercapacitor cell consisting of a positive amorphous MnO$_2$ electrode and a negative AC electrode [44]. The two cells were assembled in 0.5 M K$_2$SO$_4$ aqueous electrolyte and tested under constant current cycling [44]. The total instantaneous heat generation rate in each device was deconvoluted from the measured temperature changes [44]. In the EDLC cell, the instantaneous heat generation rates at the AC electrode half-cells were assumed to be identical [44]. In addition, the instantaneous heat generation rate at the MnO$_2$ half-cell was estimated by subtracting that measured in the AC electrode half-cell of the EDLC device from the total heat generation rate measured in the hybrid supercapacitor device [44].

More recently, Munteshari et al. [32,38] developed an isothermal *operando* calorimeter capable of measuring the instantaneous heat generation rates at each electrode of a hybrid supercapacitor using two thermoelectric heat flux sensors attached to the back of each electrode. The authors investigated a hybrid supercapacitor device consisting of a MnO$_2$ birnessite nanoparticles synthesized in a suspension of graphene (MnO$_2$-G) using microwave synthesis as a positive electrode and a negative AC electrode in 0.5 M Na$_2$SO$_4$ aqueous electrolyte [32]. Moreover, two hybrid supercapacitor devices consisting of a positive AC electrode and a MoO$_2$-nanoparticles deposited on reduced graphene oxide (MoO$_2$-rGO) as a negative electrode in EC:DMC (1:1 vol ratio) solvent with 1 M LiClO$_4$ and in EC:DMC (1:1 wt ratio) solvent with 1 M TBABF$_4$ were also investigated [32]. The devices were subjected to galvanostatic cycling with imposed current I ranging from 2 to 6 mA and potential window $\Delta\psi_s$ between $\psi_{s,min}$ = 0.4 V and $\psi_{s,max}$ = 1.4 V for the device with a MnO$_2$-G electrode and $\psi_{s,min}$ = 0.5 V and $\psi_{s,max}$ = 2.5 V for the device with a MoO$_2$-rGO electrode. The time-averaged heat generation rate at the AC electrodes was proportional to I^2 and dominated by Joule heating. Similar results were found experimentally for AC electrodes in EDLCs with various electrolytes [38,39,44,49,50]. Moreover, the time-averaged heat generation rate at the pseudocapacitive electrodes exceeded Joule heating due to irreversible heating associated with faradaic reactions and EDL formation hysteresis at the pseudocapacitive electrode [32]. The reversible heat generation rate at the AC electrodes was exothermic during charging and attributed EDL formation and endothermic during discharging due to EDL dissolution. Indeed, heat is released during the EDL formation and consumed during its dissolution as corroborated by numerical simulations [51]. By contrast, the reversible heat generation rate at the pseudocapacitive MnO$_2$-G electrode was endothermic during charging and attributed to redox reactions and desorption of cations while it was exothermic during discharging due to the spontaneous fast surface redox reactions accompanied by cations adsorption [32]. Indeed, spontaneous processes are typically exothermic while non-spontaneous

processes are endothermic [32]. On the other hand, the reversible heat generation rate at the pseudocapacitive MoO_2-rGO electrode in $LiClO_4$ in EC:DMC was endothermic during charging and attributed to the fast intercalation of small Li^+ cations and exothermic during discharging due to fast deintercalation of cations [32]. Finally, the reversible heat generation rate at the MoO_2-rGO electrode in $TBABF_4$ in EC:DMC was exothermic during charging due to the exothermic EDL formation resulting from the large TBA^+ cations being unable to intercalate into the electrode and endothermic during discharging due to the endothermic EDL dissolution [32]. These results provide a guideline for the interpretation of measured thermal signatures associated with physical and electrochemical phenomena occurring in hybrid supercapacitors during operation.

Finally, Hess et al. [43] developed an open in situ STA cell to measure simultaneously the heat flow, mass loss, resistance, and capacitance of an EDLC cell during cycling or float tests. The STA cell was designed to be used in existing STA devices combining thermogravimetric analysis (TGA), differential thermal analysis (DTA), and differential scanning calorimetry (DSC). The EDLC cell consisted of two AC electrodes with Al foil current collector separated by a glass fiber separator impregnated with 1 M $Pyr_{14}BF_4$ in PC [43]. The larger cumulative heat generation and loss of mass at higher cell voltage were consistent with the faster decrease in capacitance attributed to the electrolyte decomposition and evaporation [43].

2.4. Thermal signature of electrolyte decomposition

During cyclic voltammetry of hybrid supercapacitors, water electrolysis is endothermic and may be accompanied by a significant increase in electrical current [15]. Munteshari et al. [42] investigated two EDLC devices under a large potential window $\Delta\psi_s$ up to 4 V. The devices consisted of two AC electrodes in neat ionic liquid $Pyr_{14}TFSI$ (Device 1) or 1 M $Pyr_{14}TFSI$ diluted in PC (Device 2) [42]. Here, a rapid increase in current was observed near the end of the charging step in CV measurements for Device 2 and for the cell potential windows above 3.0 V. It was associated with PC decomposition. In fact, an endothermic dip was observed in the instantaneous heat generation rates measured at the negative electrode and was associated with PC decomposition [42]. Device 1 did not exhibit such behavior due to the absence of PC solvent in the neat ionic liquid [42]. Moreover, the electrochemical stability window of solvents decreased with increasing temperature as the contribution of thermal potential became non-negligible [52]. This has been widely used in hydrogen production where the required power input significantly decreases due to the contribution of heat to the overall energy required for electrolysis [52].

Moreover, previous calorimetric studies investigated the instantaneous heat generation rates in hybrid supercapacitor devices consisting of a positive MnO_2-based amorphous or birnessite electrode and a negative AC electrode with either 0.5 M K_2SO_4 [44] or 0.5 M Na_2SO_4 [32] aqueous electrolyte under galvanostatic cycling. However, the operating potential window of 1.0 V was too small to observe electrolysis.

The present study aims to assess the effect of electrolyte on the operating potential windows of hybrid supercapacitors with an α-MnO_2 positive electrode and an AC negative electrode. The two aqueous electrolytes (0.5 M K_2SO_4 or 0.5 M Cs_2SO_4) were selected based on their solubility in water and their ability to maintain the pH of the electrolytes close to neutral. Moreover, the size of cations and the thickness of their solvation shell were significantly different so as to isolate their importance in the early onset of hydrolysis.

3. Materials and methods

3.1. Electrode fabrication and device assembly

In order to fabricate the α-MnO_2 pseudocapacitive electrodes and the AC electrodes necessary for our study, two different slurries were prepared by mixing the active materials with carbon black (Superior Graphite, > 99%) into polyvinylidene fluoride (PVDF, Solef® 5130) binder solution in a 70:15:15 weight ratio. The active materials were cryptomelane α-MnO_2 (Prince Erachem) and activated carbon (YP-50F, Kuraray Chemical). The PVDF solution was prepared by dissolving PVDF powder in liquid dimethylacetamide (DMA) in an 8.5:91.5 weight ratio. Dry matter contents of the active materials were respectively adjusted at 25.3 wt% and 18.7 wt% for α-MnO_2 and AC slurries by adding DMA in order to obtain homogeneous mixtures after vigorous stirring overnight with a magnetic stirrer.

The slurries were drop cast onto titanium (Ti) mesh current collector sheets (Dexmet Corp.) with a 1×1 cm^2 footprint area and spread evenly with a spatula. The Ti mesh had been previously treated in a boiling aqueous solution containing 10 wt% of oxalic acid for at least 30 min and rinsed off with DI water in order to enhance the adhesion between the slurry and the mesh current collector. The electrodes were dried in an oven at 60 °C for 12 h. Then, all the electrodes were hot-roll calendared to ensure that the thickness was uniform over the entire electrode and ranged between 36 and 51 μm for α-MnO_2 electrodes and between 82 and 96 μm for AC electrodes [53]. This resulted in a mass loading of 5–7 mg/cm^2 for both types of electrodes.

Finally, the devices were assembled with a positive α-MnO_2 electrode and a negative AC electrode separated by a 1 mm-thick, chemically inert, polypropylene mesh separator. The separator was impregnated with either 0.5 M K_2SO_4 (Device 1) or 0.5 M Cs_2SO_4 (Device 2) aqueous electrolytes. These electrolytes were chosen for their significantly different solvation shell thickness [54,55], relatively small ion hydration molar enthalpy to ensure that ion hydration does not dominate heat generation, and sufficiently large solubility in water (>0.5 M) to achieve good capacity. Table 1 summarizes the electrode and electrolyte properties including parameters used in the interpretation of the results including the active mass loading of the electrodes m_{MnO_2} and m_{AC}, the unsolvated $a_{+/-}$ and solvated $a_{+/-,s}$ ion diameters, their diffusion coefficients $D_{+/-}$, and the ion hydration molar enthalpies $\Delta H_{sol,+/-}$.

3.2. Electrochemical characterization

First, the positive α-MnO_2 and the negative AC working electrodes were tested separately in a three electrode setup using elemental Ni as the counter electrode and $Ag^+/AgCl$ as the reference electrode (Fisherbrand™ accumet™). Each working electrode was subjected to cyclic voltammetry (CV) at scan rate $v = 10$ mV/s for 95 cycles and then at scan rate $v = 5$ mV/s for the last 5 cycles, with potential window ranging between $\psi_{min} = -0.8$ V and $\psi_{max} = 0$ V for the AC electrode and $\psi_{min} = 0$ V and $\psi_{max} = 0.8$ V for the α-MnO_2 electrode. The measured cyclic voltammograms were then used to determine the capacity of each electrode in K_2SO_4 and Cs_2SO_4 aqueous electrolytes so as to pair the α-MnO_2 and AC electrodes with matched capacity in a hybrid device. Here, as argued in Ref. [14], the capacity (in mAh) was chosen in favor of capacitance (in F) as surface redox reactions are the predominant charge storage mechanism [24]. The capacity $C(v)$ (in C) as a function of scan rate v was defined as [56],

$$C(v) = \oint \frac{I(\psi_s)}{2v} d\psi_s. \tag{6}$$

Here, $I(\psi_s)$ is the measured current response at the triangular cell potential $\psi_s(t)$. The capacity $C(v)$ in mAh can be converted to Coulomb (C) by multiplying it by a factor 3.6.

Second, CV measurements were performed on the assembled devices inside the calorimetric cell for 30 cycles at five different scan rates v ranging from 5 to 50 mV/s at 20 °C. Here, the potential window $\Delta\psi_s$ ranged between $\psi_{s,min} = 0$ V, and $\psi_{s,max} = 1.6$ V. The gravimetric capacity $C_g(v)$ (in mAh/g) of the devices was also computed according to

$$C_g(v) = \frac{C(v)}{m} \tag{7}$$

Table 1
Electrode and electrolyte properties of the hybrid supercapacitors investigated.

Property/parameter	Device 1	Device 2
Electrolyte (0.5 M in DI water)	K_2SO_4	Cs_2SO_4
Active mass loading of α-MnO_2, m_{MnO_2} (mg)	6.09	5.53
Active mass loading of AC, m_{AC} (mg)	5.99	5.33
Electrolyte pH	6.69	6.55
Cation diameter, a_+ (nm) [54]	0.276	0.334
Solvated cation diameter, $a_{+,s}$ (nm) [55]	0.315	0.346
Anion diameter, a_- (nm)[61]	0.484	0.484
Solvated anion diameter, $a_{-,s}$ (nm) [61]	1.173	1.173
Cation diffusion coefficient, $D_+ \times 10^9$ (m^2/s) [62]	2.135	2.076
Anion diffusion coefficient, $D_- \times 10^9$ (m^2/s) [63]	0.809	0.809
Cation hydration molar enthalpy, $\Delta H_{sol,+}$ (kJ/mol) [64]	−322	−264
Anion hydration molar enthalpy, $\Delta H_{sol,-}$ (kJ/mol) [64]	−1059	−1059
Device internal resistance, R_s (Ω)	10.89	9.96

where m (in g) is the mass loading of active material in both α-MnO_2 and AC electrodes reported in Table 1.

Furthermore, galvanostatic cycling combined with isothermal calorimetric measurements were performed on the devices at constant current I equal to 5 mA and 6 mA. Here, the cell potential window $\Delta\psi_s$ was first set to 1.2 V to ensure that no hydrolysis occurred. It was then gradually increased to 1.6 V, 1.8 V, and up to 2.0 V until hydrolysis was observed. For each imposed current I, thirty consecutive cycles were performed to ensure that an oscillatory steady-state in the measured heat generation rates had been reached.

Finally, the internal resistance of the device R_s was computed from the IR drop observed at the transition between the charging and discharging steps during galvanostatic cycling according to [57–60],

$$R_s(I) = \frac{\psi_s(t_c^+) - \psi_s(t_c^-)}{2I}. \tag{8}$$

Here, $\psi_s(t_c^+)$ and $\psi_s(t_c^-)$ were the cell potentials at the end of the charging step and 10 ms after the beginning of the discharging step, respectively (i.e., $t_c^+ - t_c^- = 10$ ms), as recommended in Ref. [58].

3.3. Isothermal operando calorimeter

The instantaneous heat generation rate at each electrode in Devices 1 and 2 was measured during galvanostatic cycling for current $I = 5$ and 6 mA and potential window $\Delta\psi_s = 1.2$, 1.6, 1.8 V, and up to 2.0 V. The instantaneous heat generation rate $\dot{Q}_i(t)$ (in mW) at electrode i ($i = \alpha$-MnO_2 or AC) was obtained from the heat flux $q_i''(t)$ measured by the thermoelectric heat flux sensor in thermal contact with the electrode according to [38],

$$\dot{Q}_i = q_i''(t)A_i = \frac{\Delta V_i(t)}{S_i}A_i. \tag{9}$$

Here, A_i denotes the footprint area of the electrode ($A_i = 1$ cm^2), ΔV_i is the instantaneous voltage difference measured at each heat flux sensor in thermal contact with electrode i while S_i is the temperature-dependent sensitivity (in μV/(W/m^2)) provided by the manufacturer.

Finally, in an effort to reduce the noise in the measurements, the instantaneous heat generation rate at electrode i was averaged over the last five cycles of the 30 cycles as

$$\dot{Q}_i(t) = \frac{1}{5}\sum_{j=26}^{30} \dot{Q}_i(t + (j-1)t_{cd}), \tag{10}$$

where t_{cd} is the period of one cycle and j is the cycle number ($j = 26$ to 30).
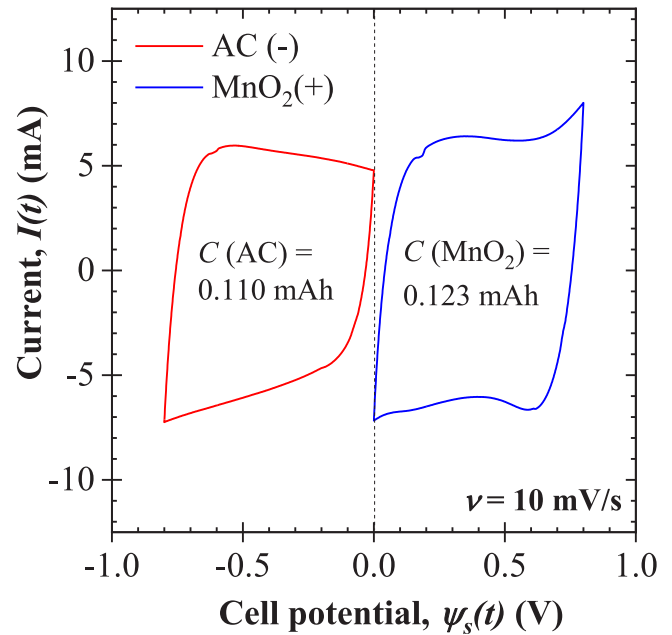
4. Results and discussion

4.1. Cyclic voltammetry

4.1.1. Three-electrode setup

Fig. 1 shows the measured cyclic voltammograms for the positive α-MnO_2 and the negative AC electrodes vs. Ag$^+$/AgCl reference electrode
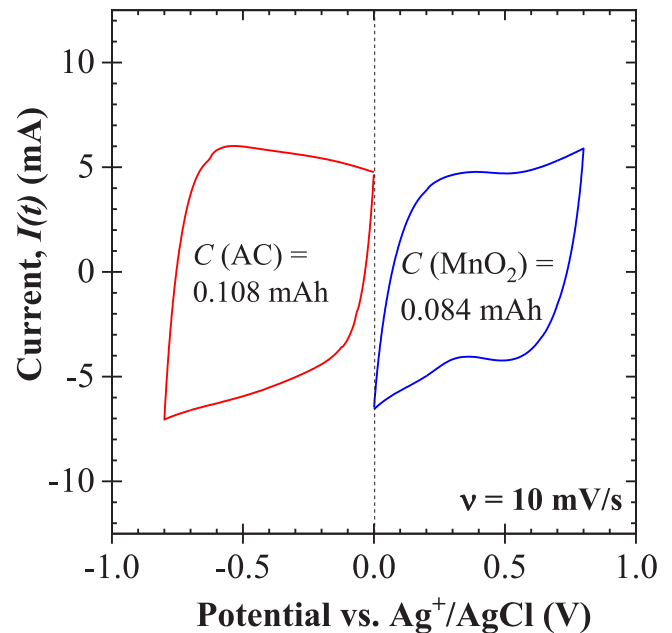

Fig. 1. Cyclic voltammograms for individual AC and cryptomelane α-MnO_2 electrodes vs. Ag$^+$/AgCl reference electrode in (a) 0.5 M K_2SO_4 and (b) 0.5 M Cs_2SO_4 aqueous electrolytes at scan rate $v = 10$ mV/s.

in (a) 0.5 M K_2SO_4 and (b) 0.5 M Cs_2SO_4 aqueous electrolytes at scan rate $v = 10$ mV/s. These CV curves were used to compute the capacity $C(v)$ of each electrode according to Eq. (6). The AC electrodes had similar mass loading (Table 1) and exhibited similar behavior in the two different electrolytes. Their capacity was about 0.11 mAh. Moreover, the α-MnO_2 electrodes exhibited an oxidation peak at the end of the positive sweep at $\psi_s \simeq 0.8$ V vs. Ag$^+$/AgCl in all electrolytes. A reduction dip at the start of the negative sweep was also observed at $\psi_s \simeq 0.6$ V vs. Ag$^+$/AgCl. The positive and negative electrodes were

(a) Device 1 (0.5 M K$_2$SO$_4$)

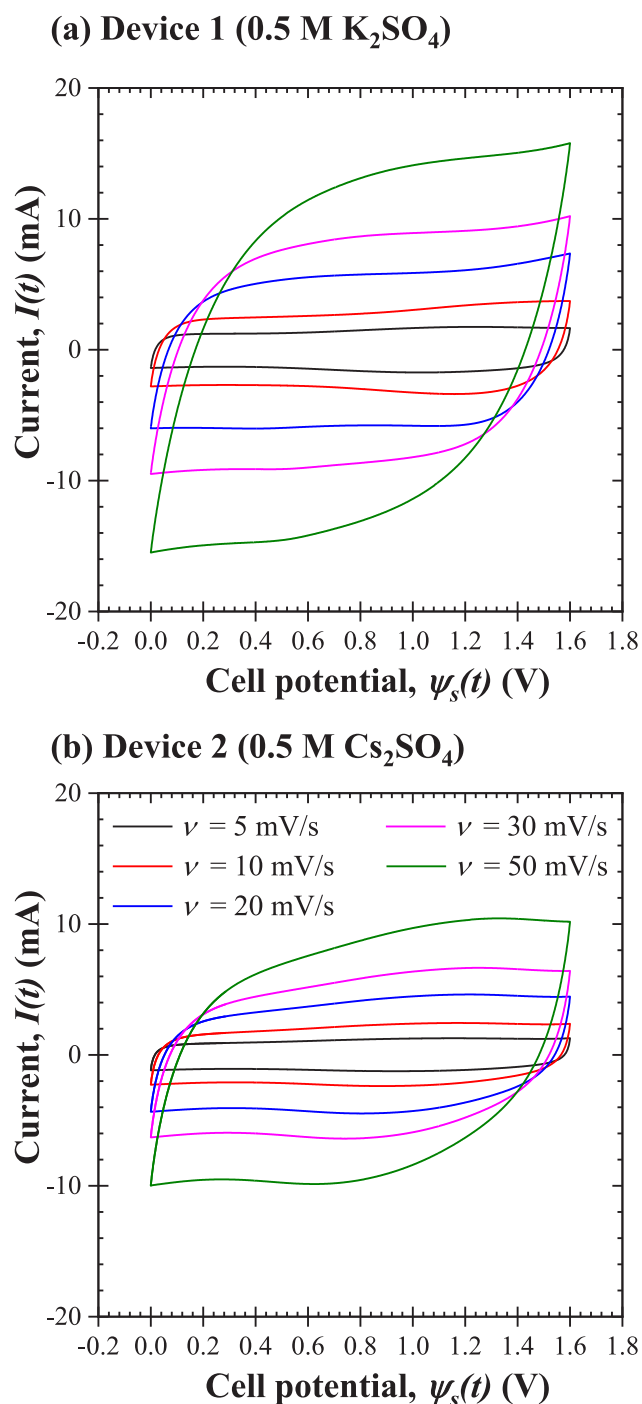## (b) Device 2 (0.5 M Cs$_2$SO$_4$)

Fig. 2. Cyclic voltammograms as functions of scan rate ν = 5 to 50 mV/s for (a) Device 1 with 0.5 M K$_2$SO$_4$ and (b) Device 2 with 0.5 M Cs$_2$SO$_4$ aqueous electrolytes.
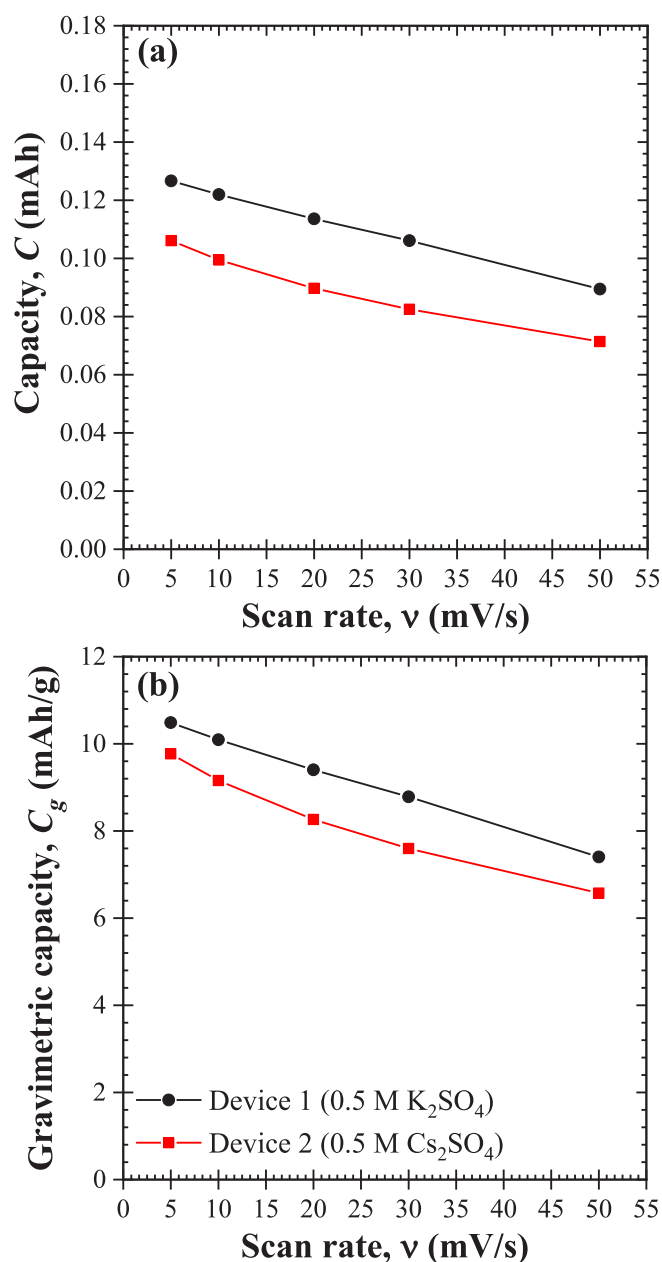

Fig. 3. (a) Capacity $C(\nu)$ and (b) gravimetric capacity $C_g(\nu)$ per unit mass of both electrodes as functions of scan rate ν for Device 1 with 0.5 M K$_2$SO$_4$ and Device 2 with 0.5 M Cs$_2$SO$_4$ aqueous electrolytes.

paired so that their capacity was similar in each device. Note that no gas (H$_2$ or O$_2$) evolution or bubble formation was visible at either electrode during cycling.

4.1.2. Full device setup

Fig. 2 shows the measured cyclic voltammograms for (a) Device 1 with 0.5 M K$_2$SO$_4$ and (b) Device 2 with 0.5 M Cs$_2$SO$_4$ aqueous electrolytes for scan rate ν varying from 5 to 50 mV/s. The cell potential $\psi_s(t)$ was measured at the positive α-MnO$_2$ electrode with respect to the negative AC electrode. The CV curves for both devices changed from a rectangular shape at low scan rates to a leaf-like shape at

higher scan rates, indicative of resistive behavior. Moreover, although the cell potential window of $\Delta\psi_s$ = 1.6 V exceeded the theoretical electrochemical stability window of 1.23 V for water in both devices, no evidence of hydrolysis could be observed in the CV curves [65,66].

Moreover, Fig. 3 shows (a) the capacity $C(\nu)$ and (b) the gravimetric capacity $C_g(\nu)$ per unit mass of both electrodes as functions of scan rate ν for Devices 1 and 2. For both devices, the capacity $C(\nu)$ and the gravimetric capacity $C_g(\nu)$ decreased with increasing scan rate. This can be attributed to ion diffusion limitations and the slow surface redox reactions, as observed in previous experimental studies [32,67–69]. Similar trends and values of gravimetric capacity $C_g(\nu)$ as a function of scan rate ν were also reported by Boisset et al. [48]. Rate capability and capacity retention of electrodes made of MnO$_2$ nanoparticles were reported in Ref. [67]. Furthermore, the gravimetric capacity $C_g(\nu)$ was larger for Device 1 (0.5 M K$_2$SO$_4$) than for Device 2 (0.5 M Cs$_2$SO$_4$).
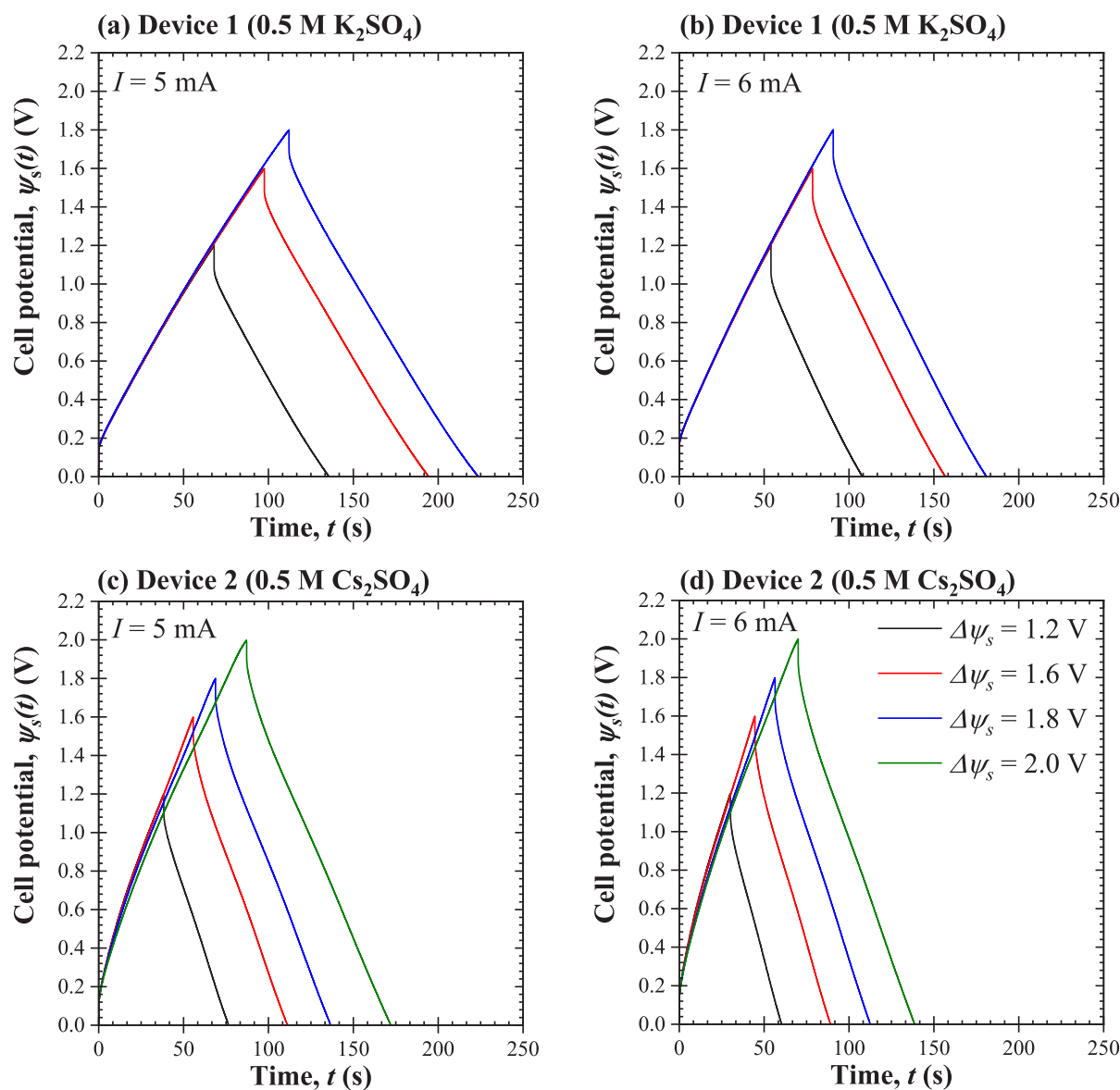
Fig. 4. Temporal evolution of the cell potential $\psi_s(t)$ during galvanostatic cycling with constant current I of 5 mA and 6 mA (a, b) for Device 1 with 0.5 M K$_2$SO$_4$ and (c, d) for Device 2 with 0.5 M Cs$_2$SO$_4$ aqueous electrolytes and for potential windows $\Delta\psi_s$ ranging from 1.2 V to 2.0 V.

This can be attributed to the larger mass loading of both electrodes in Device 1 (0.5 M K$_2$SO$_4$) than in Device 2 (0.5 M Cs$_2$SO$_4$). This resulted in more active material (i.e., α-MnO$_2$ or AC) in the electrode and larger surface area available for surface redox or EDL formation.

4.2. Galvanostatic cycling

Fig. 4 shows the temporal evolution of the cell potential $\psi_s(t)$ under galvanostatic cycling for two different currents I = 5 or 6 mA and different potential windows varying (a, b) from $\Delta\psi_s$ = 1.2 to 1.8 V for Device 1 and (c, d) from $\Delta\psi_s$ = 1.2 to 2.0 V for Device 2. For both devices, the cell potential $\psi_s(t)$ varied almost linearly with time t except at the beginning of the charging or discharging steps featuring an IR drop. A similar behavior can be observed in many EDLCs and hybrid supercapacitors with surface redox reactions [19,41,42,70]. Here also, no electrolyte decomposition was evident in the measured cell potential $\psi_s(t)$ as the cycle period t_{cd} monotonically decreased with increasing current I. Interestingly, the galvanostatic cycle period t_{cd} was shorter for Device 2 than for Device 1, as corroborated by its smaller capacity (Fig. 3). In addition, the internal resistance R_s of each device, computed

according to Eq. (8), was independent of the imposed current I and equal to $R_s = 10.89 \pm 0.02$ Ω for Device 1 and $R_s = 9.96 \pm 0.65$ Ω for Device 2 (see Table 1). Note that the slightly larger resistance of Device 1 compared to Device 2 was due to the slightly larger mass loading of both its electrodes whereas the diffusion coefficients of K$^+$ and Cs$^+$ cations in water were similar (Table 1).

4.3. Instantaneous heat generation rate measurements

4.3.1. Negative AC electrode

Fig. 5 shows the instantaneous heat generation rate $\dot{Q}_{AC}(t)$ averaged over 5 consecutive cycles [Eq. (10)] at the negative AC electrode in (a, b) Device 1 in 0.5 M K$_2$SO$_4$ aqueous electrolyte for potential window $\Delta\psi_s$ of 1.2 V, 1.6 V, and 1.8 V and in (c, d) Device 2 in 0.5 M Cs$_2$SO$_4$ aqueous electrolyte for potential window $\Delta\psi_s$ = 1.2 V, 1.6 V, 1.8 V, and 2.0 V for imposed current I equal to (a, c) 5 mA and (b, d) 6 mA, respectively. First, the instantaneous heat generation rate at each electrode and its thermal signatures were repeatable from cycle to cycle in both devices. Then, the heat generation rates exhibited the same features for both currents and both electrolytes. A slight increase in
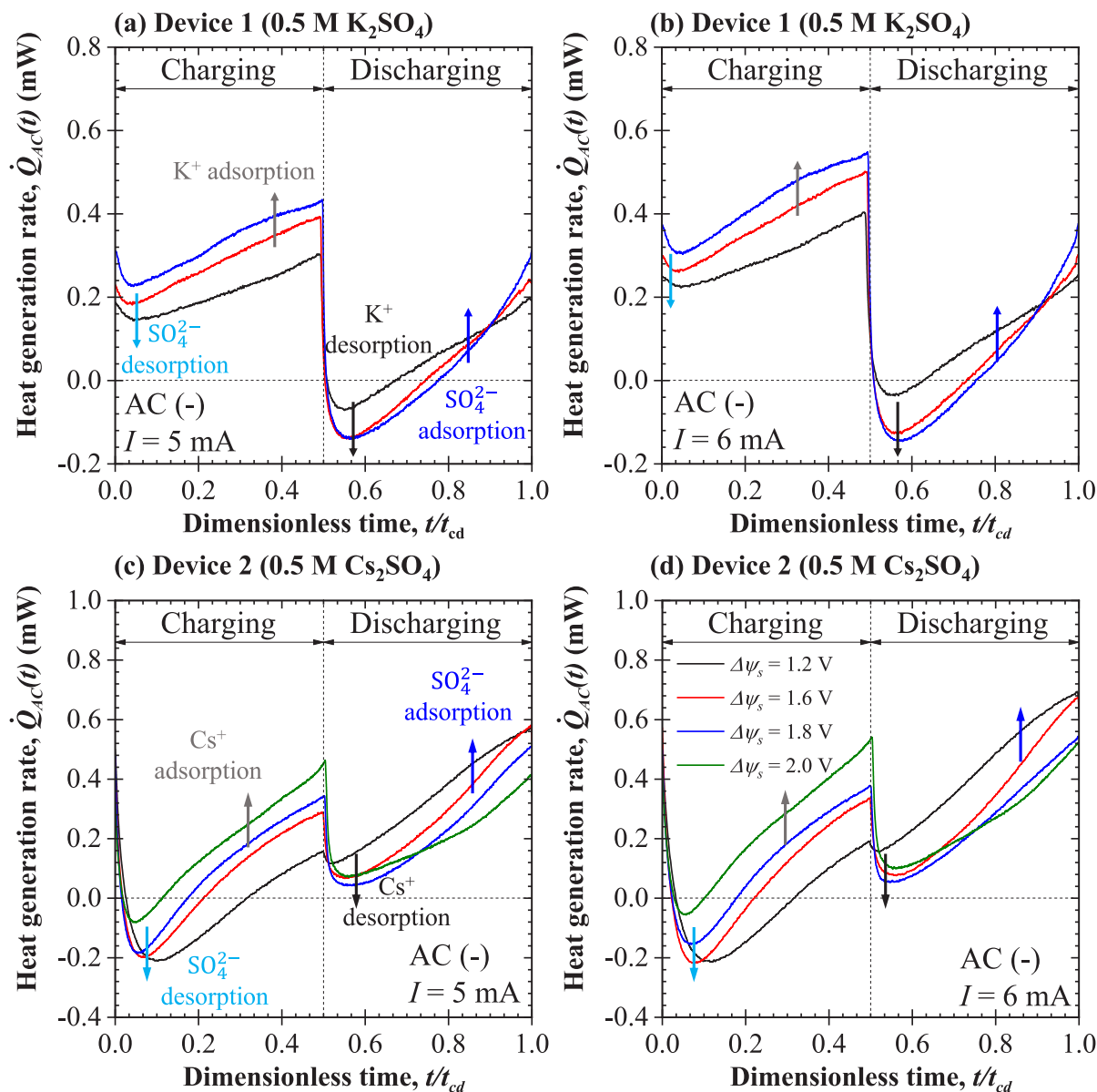
Fig. 5. Instantaneous heat generation rate at the AC electrodes (a, b) for Device 1 in 0.5 M K$_2$SO$_4$ aqueous electrolyte for potential windows $\Delta\psi_s$ = 1.2, 1.6, and 1.8 V and (c, d) for Device 2 in 0.5 M Cs$_2$SO$_4$ aqueous electrolyte for potential windows $\Delta\psi_s$ = 1.2, 1.6, 1.8, and 2.0 V as a function of dimensionless time t/t_{cd} with decreased white noise for AC electrode subjected to imposed current of (a, c) I = 5 mA and (b, d) I = 6 mA.

the heat generation rate $\dot{Q}_{AC}(t)$ was observed at the AC electrode with increasing current I due to increasing resistive losses accompanied by Joule heating. A slight endothermic dip was also observed at the AC electrode at the beginning of the charging step. It can be attributed to the endothermic desorption and solvation of SO$_4^{2-}$ anions, as previously observed [32,49]. As the charging progressed, the heat generation rate increased due to desolvation and exothermic adsorption of K$^+$ (Device 1) and Cs$^+$ (Device 2) ions in the porous AC electrode [32,49]. Furthermore, an endothermic dip was observed at the beginning of the discharging step attributed this time to the endothermic desorption and solvation of K$^+$ and Cs$^+$ cations upon reversal of the current. As the discharging step progressed, desolvation and exothermic adsorption of SO$_4^{2-}$ anions dominated for the remainder of the discharging step.

4.3.2. Positive α-MnO$_2$ electrode

Fig. 6 shows the instantaneous heat generation rate $\dot{Q}_{MnO_2}(t)$ measured at the positive α-MnO$_2$ electrode in (a, b) Device 1 in 0.5 M K$_2$SO$_4$ aqueous electrolyte for $\Delta\psi_s$ equal to 1.2 V, 1.6 V, and 1.8 V and in (c,

d) Device 2 in 0.5 M Cs$_2$SO$_4$ aqueous electrolyte for $\Delta\psi_s$ equal to 1.2 V, 1.6 V, 1.8 V, and 2.0 V and imposed current I equal to (a, c) 5 mA and (b, d) 6 mA, respectively. Here also, the instantaneous heat generation rate at each electrode and its thermal signatures were repeatable from cycle to cycle for both devices. Furthermore, the heat generation rate $\dot{Q}_{MnO_2}(t)$ exhibited the same behavior in for both currents and both electrolytes. First, $\dot{Q}_{MnO_2}(t)$ increased in magnitude with increasing current I due to the associated increase in Joule heating. In addition, at the beginning of the charging step, an endothermic dip was observed and attributed to endothermic desorption and solvation of K$^+$ (Device 1) or Cs$^+$ (Device 2), based on similar findings by Munteshari et al. [32]. As the charging progressed, exothermic SO$_4^{2-}$ adsorption and desolvation began to dominate resulting in the slow rise observed in $\dot{Q}_{MnO_2}(t)$ [32].

Interestingly, in Device 1 for potential window $\Delta\psi_s$ of 1.6 V and 1.8 V and in Device 2 for $\Delta\psi_s$ of 2.0 V a distinct endothermic dip began to appear at the end of charging for both currents considered. This dip observed at the positive electrode could be attributed to hydrolysis reaction for several reasons namely (i) hydrolysis is an endothermic
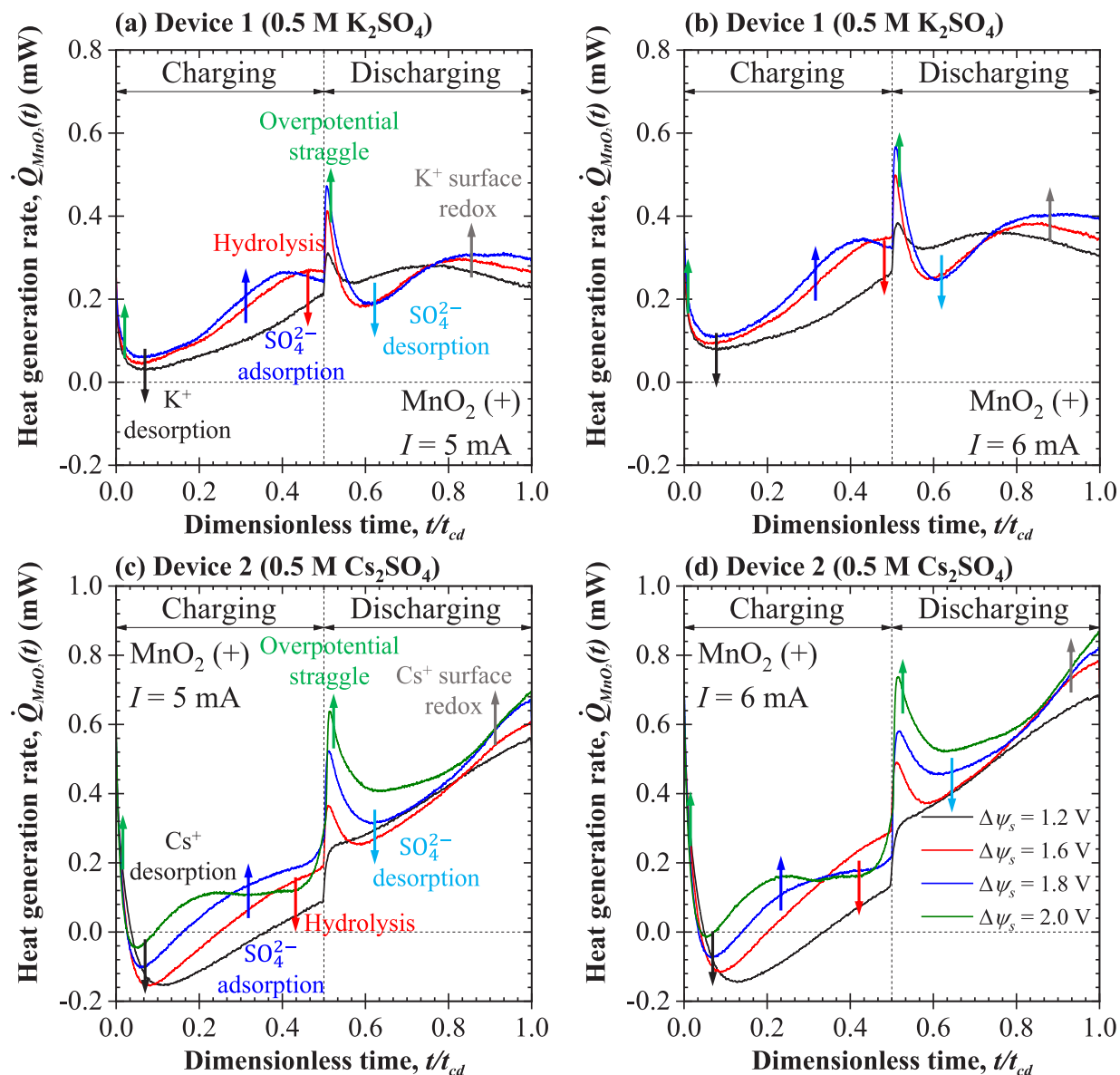
Fig. 6. Instantaneous heat generation rate at the α-MnO$_2$ electrodes (a, b) for Device 1 in 0.5 M K$_2$SO$_4$ aqueous electrolyte for potential windows $\Delta\psi_s$ = 1.2, 1.6, and 1.8 V and (c, d) for Device 2 in 0.5 M Cs$_2$SO$_4$ aqueous electrolyte for potential windows $\Delta\psi_s$ = 1.2, 1.6, 1.8, and 2.0 V as a function of dimensionless time t/t_{cd} with decreased white noise for AC electrode subjected to imposed current of (a, c) I = 5 mA and (b, d) I = 6 mA.

process [71,72], (ii) it appeared only at large potentials, (iii) it appeared at the positive electrode as the electrolyte pH was slightly basic (Table 1), and (iv) a similar dip was observed in EDLCs and attributed to PC decomposition at potential windows above 3 V. Interestingly, the thermal signature of the onset of hydrolysis could only be observed via *operando* calorimetric measurements at the positive electrode while it was not apparent in any electrochemical measurements (Figs. 2 and 4).

Moreover, the onset of hydrolysis occurred at a higher cell potential window $\Delta\psi_s$ for Cs$_2$SO$_4$ than for K$_2$SO$_4$ aqueous electrolyte. This may be attributed to the thinner solvation shell forming around Cs$^+$ cations [55]. The thin solvation shell combined with desolvation of Cs$^+$ cations undergoing surface redox led to a lack of water molecules near the electrode surface where the potential was the largest. Although the electric potential may exceed the theoretical water electrochemical stability window of 1.23 V close to the electrode, hydrolysis cannot occur in the absence of water molecules. Similar delay in the onset of hydrolysis was observed by Suo et al. [35] using WISE systems in Li ion batteries with LiMn$_2$O$_4$-based cathode and Mo$_6$S$_8$-based anode.

Furthermore, in both devices at the beginning of the discharging step, a short spike in $\dot{Q}_{MnO_2}(t)$ appeared immediately after the current I switched from positive to negative. It was attributed to a straggle in the surface overpotential responsible for resistive losses and Joule heating as the current switched from positive to negative [73]. This behavior was more pronounced for larger potential windows when the straggle in overpotential was larger [73]. Such behavior was previously observed in numerical simulations [73] as well as experimentally [44]. Interestingly, this behavior could also be observed in the beginning of charging as the initially exothermic heat generation at $t/t_{cd} \simeq 0$. After the initial spike in heat generation rate, an endothermic dip caused by the endothermic desorption and solvation of the SO$_4^{2-}$ ions accumulated during charging. Finally, $\dot{Q}_{MnO_2}(t)$ increased in the second part of the discharging step due to desolvation and exothermic surface redox involving K$^+$ (Device 1) or Cs$^+$ (Device 2) ions. This contribution started intensely and later decreased in intensity as the conditions became less favorable for surface redox reactions. This too was in agreement with previously reported experimental studies [32,44] and numerical predictions [73].
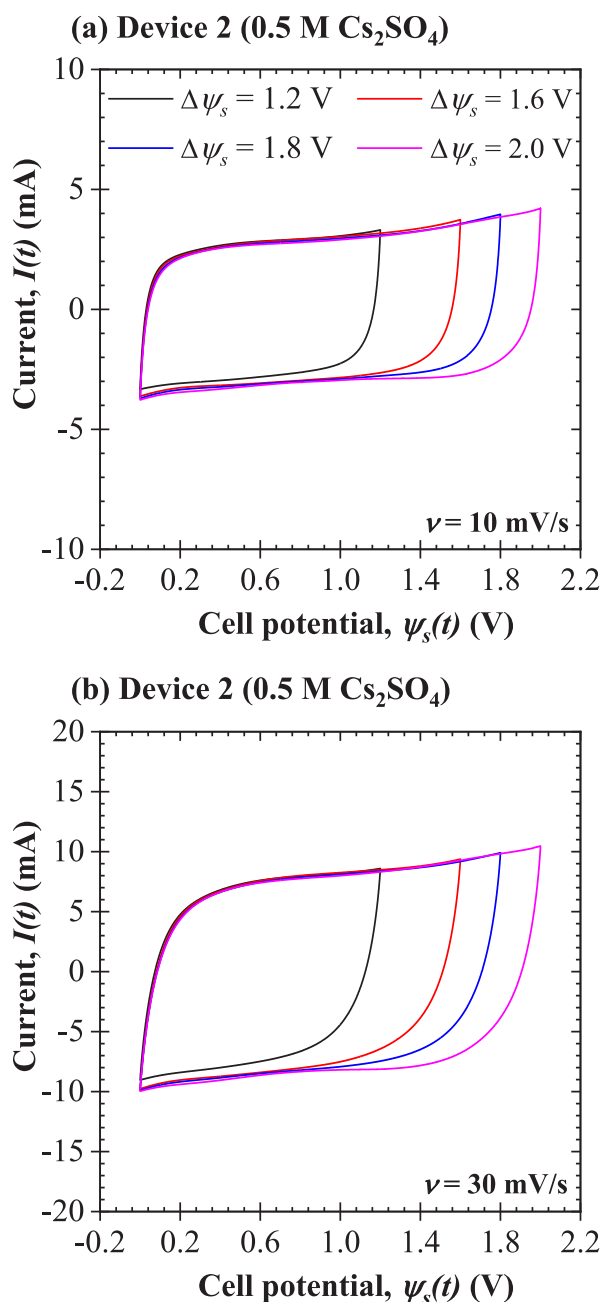
(a) Device 2 (0.5 M Cs$_2$SO$_4$)

(b) Device 2 (0.5 M Cs$_2$SO$_4$)

Fig. 7. Cyclic voltammograms for Device 2 in 0.5 M Cs$_2$SO$_4$ aqueous electrolyte for potential windows $\Delta\psi_s$ = 1.2, 1.6, 1.8 V, and 2.0 V for scan rate (a) ν = 10 mV/s, and (b) ν = 30 mV/s after CV, GC, and calorimetric measurements.

Additional cyclic voltammetry measurements were performed on Device 2, after 30 galvanostatic cycles performed during *operando* calorimetry. Fig. 7 shows the measured cyclic voltammograms for scan rate (a) ν = 10 and (b) ν = 30 mV/s for potential window ranging from 1.2 V to 2.0 V. For both scan rates ν, no sharp rise in current at high cell potential voltage ψ_s, often associated with hydrolysis reaction, was observed [41,42,65]. This unequivocally establishes that the early onset of hydrolysis could be observed with isothermal *operando* calorimetry before it could be observed with electrochemical measurements.

5. Conclusion

This study reported measurements of the instantaneous heat generation rates at the positive α-MnO$_2$ cryptomelane and negative AC electrodes in hybrid supercapacitors with either 0.5 M K$_2$SO$_4$ or 0.5 M Cs$_2$SO$_4$ aqueous electrolytes with pH of 6.69 and 6.55, respectively. The measurements were performed in an *operando* isothermal calorimeter under galvanostatic cycling with potential window up to 1.8 V for the device with K$_2$SO$_4$ aqueous electrolyte and up to 2.0 V for the device with Cs$_2$SO$_4$ aqueous electrolyte. An endothermic dip observed at the AC electrodes in the beginning of the charging step was caused by anion desorption and solvation. Similar dips were observed at the α-MnO$_2$ electrodes also caused by cation and anion desorption and solvation. By contrast, exothermic peaks at the α-MnO$_2$ electrodes were attributed to cation surface redox, anion adsorption and desolvation, and overpotential straggle. Moreover, in both devices, an endothermic dip was observed at the positive electrode at the end of the charging step for the largest potential windows and was attributed to hydrolysis reaction. Interestingly, the onset of hydrolysis occurred at higher potentials significantly above 1.23 V in electrolytes with cations featuring a thinner solvation shell. Finally, the onset of hydrolysis could be detected by calorimetry before it could manifest itself in electrochemical measurements. Indeed, as the cell potential window was increased, the current remained small. However, hydrolysis is strongly endothermic and its thermal signature could be identified by the high sensitivity heat flux sensor in thermal contact with the positive α-MnO$_2$ electrode.

CRediT authorship contribution statement

Matevž Frajnkovič: Conceptualization, Data curation, Formal analysis, Investigation, Visualization, Writing – original draft, Writing – review & editing. **Ampol Likitchatchawankun:** Conceptualization, Formal analysis, Writing – review & editing. **Camille Douard:** Conceptualization, Formal Analysis, Writing – review & editing. **Yucheng Zhou:** Conceptualization, Data curation, Investigation, Writing – review & editing. **Sun Woong Baek:** Writing – review & editing. **Ivan Catton:** Supervision. **Olivier Crosnier:** Conceptualization, Supervision, Writing – review & editing. **Thierry Brousse:** Conceptualization, Supervision, Writing – review & editing. **Laurent Pilon:** Conceptualization, Project administration, Supervision, Writing – review & editing.

Declaration of competing interest

The authors declare that they have no known competing financial interests or personal relationships that could have appeared to influence the work reported in this paper.

Data availability

Data will be made available on request.

References

[1] M. Winter, R.J. Brodd, What are batteries, fuel cells, and supercapacitors? Chem. Rev. 104 (10) (2004) 4245–4270.

[2] K. Naoi, P. Simon, New materials and new configurations for advanced electrochemical capacitors, Electrochem. Soc. Interface 17 (1) (2008) 34–37.

[3] D.P. Dubal, O. Ayyad, V. Ruiz, P. Gómez-Romero, Hybrid energy storage: the merging of battery and supercapacitor chemistries, Chem. Soc. Rev. 44 (7) (2015) 1777–1790.

[4] J. McDowall, Conventional battery technologies-present and future, in: Proc. 2000 IEEE Power Engineering Society Summer Meeting, Vol. 3, IEEE, 2000, pp. 1538–1540.

[5] Y. Nishi, Lithium ion secondary batteries; past 10 years and the future, J. Power Sources 100 (1–2) (2001) 101–106.

[6] T. Osaka, M. Datta (Eds.), Energy Storage Systems in Electronics, CRC Press, Boca Raton, FL, 2000, URL https://www.ebook.de/de/product/37645921/ energy_storage_systems_in_electronics.html.

[7] Y. Gogotsi, P. Simon, True performance metrics in electrochemical energy storage, Science 334 (6058) (2011) 917–918.

[8] K. Naoi, S. Ishimoto, J. Miyamoto, W. Naoi, Second generation 'nanohybrid supercapacitor': Evolution of capacitive energy storage devices, Energy Environ. Sci. 5 (11) (2012) 9363–9373.

[9] H. Shi, Activated carbons and double layer capacitance, Electrochim. Acta 41 (10) (1996) 1633–1639.

[10] D. Lozano-Castelló, D. Cazorla-Amorós, A. Linares-Solano, S. Shiraishi, H. Kurihara, A. Oya, Influence of pore structure and surface chemistry on electric double layer capacitance in non-aqueous electrolyte, Carbon 41 (9) (2003) 1765–1775.

[11] E. Raymundo-Piñero, K. Kierzek, J. Machnikowski, F. Béguin, Relationship between the nanoporous texture of activated carbons and their capacitance properties in different electrolytes, Carbon 44 (12) (2006) 2498–2507.

[12] P. Simon, A. Burke, Nanostructured carbons: Double-layer capacitance and more, Electrochem. Soc. Interface 17 (1) (2008) 38–43.

[13] L.L. Zhang, X.S. Zhao, Carbon-based materials as supercapacitor electrodes, Chem. Soc. Rev. 38 (9) (2009) 2520–2531.

[14] T. Brousse, D. Bélanger, J.W. Long, To be or not to be pseudocapacitive? J. Electrochem. Soc. 162 (5) (2015) A5185–A5189.

[15] M.S. Hong, S.H. Lee, S.W. Kim, Use of KCl aqueous electrolyte for 2 V manganese oxide/activated carbon hybrid capacitor, Electrochem. Solid-State Lett. 5 (10) (2002) A227–A230.

[16] T. Brousse, M. Toupin, D. Bélanger, A hybrid activated carbon-manganese dioxide capacitor using a mild aqueous electrolyte, J. Electrochem. Soc. 151 (4) (2004) A614–A622.

[17] T. Brousse, D. Bélanger, A hybrid fe_3o_4-MnO_2 capacitor in mild aqueous electrolyte, Electrochem. Solid-State Lett. 6 (11) (2003) A244.

[18] B. Conway, V. Birss, J. Wojtowicz, The role and utilization of pseudocapacitance for energy storage by supercapacitors, J. Power Sources 66 (1–2) (1997) 1–14.

[19] M.R. Lukatskaya, B. Dunn, Y. Gogotsi, Multidimensional materials and device architectures for future hybrid energy storage, Nature Commun. 7 (1) (2016).

[20] P. Simon, Y. Gogotsi, B. Dunn, Where do batteries end and supercapacitors begin? Science 343 (6176) (2014) 1210–1211.

[21] W.G. Pell, B.E. Conway, Peculiarities and requirements of asymmetric capacitor devices based on combination of capacitor and battery-type electrodes, J. Power Sources 136 (2) (2004) 334–345.

[22] J.P. Zheng, The limitations of energy density of battery/double-layer capacitor asymmetric cells, J. Electrochem. Soc. 150 (4) (2003) A484.

[23] V. Augustyn, P. Simon, B. Dunn, Pseudocapacitive oxide materials for high-rate electrochemical energy storage, Energy Environ. Sci. 7 (5) (2014) 1597–1614.

[24] T. Brousse, D. Belanger, K. Chiba, M. Egashira, F. Favier, J. Long, J.R. Miller, M. Morita, P.S. K. Naoi, W. Sugimoto, Chapter 16: materials for electrochemical capacitors, in: Springer Handbook of Electrochemical Energy, Springer, Berlin, Germany, 2017, pp. 495–561.

[25] M. Toupin, T. Brousse, D. Bélanger, Charge storage mechanism of MnO_2 electrode used in aqueous electrochemical capacitor, Chem. Mater. 16 (16) (2004) 3184–3190.

[26] Y. Zhu, L. Peng, D. Chen, G. Yu, Intercalation pseudocapacitance in ultrathin $VOPO_4$ nanosheets: Toward high-rate alkali-ion-based electrochemical energy storage, Nano Lett. 16 (1) (2015) 742–747.

[27] S.-B. Ma, K.-Y. Ahn, E.-S. Lee, K.-H. Oh, K.-B. Kim, Synthesis and characterization of manganese dioxide spontaneously coated on carbon nanotubes, Carbon 45 (2) (2007) 375–382.

[28] D. Choi, G.E. Blomgren, P.N. Kumta, Fast and reversible surface redox reaction in nanocrystalline vanadium nitride supercapacitors, Adv. Mater. 18 (9) (2006) 1178–1182.

[29] J.R. Miller, P. Simon, Electrochemical capacitors for energy management, Science 321 (5889) (2008) 651–652.

[30] W. Sugimoto, T. Kizaki, K. Yokoshima, Y. Murakami, Y. Takasu, Evaluation of the pseudocapacitance in ruo_2 with a ruo_2/GC thin film electrode, Electrochim. Acta 49 (2) (2004) 313–320.

[31] V. Augustyn, J. Come, M.A. Lowe, J.W. Kim, P.-L. Taberna, S.H. Tolbert, H.D. Abruna, P. Simon, B. Dunn, High-rate electrochemical energy storage through Li^+ intercalation pseudocapacitance, Nature Mater. 12 (6) (2013) 518–522.

[32] O. Munteshari, J. Lau, A. Likitchatchawankun, B.-A. Mei, C.S. Choi, D. Butts, B. Dunn, L. Pilon, Thermal signature of ion intercalation and surface redox reactions mechanisms in model pseudocapacitive electrodes, Electrochim. Acta 307 (2019) 512–524.

[33] V. Khomenko, E. Raymundo-Piñero, F. Béguin, Optimisation of an asymmetric manganese oxide/activated carbon capacitor working at 2 V in aqueous medium, J. Power Sources 153 (1) (2006) 183–190.

[34] L. Demarconnay, E. Raymundo-Piñero, F. Béguin, Adjustment of electrodes potential window in an asymmetric carbon/MnO_2 supercapacitor, J. Power Sources 196 (1) (2011) 580–586.

[35] L. Suo, O. Borodin, T. Gao, M. Olguin, J. Ho, X. Fan, C. Luo, C. Wang, K. Xu, "Water-in-salt" electrolyte enables high-voltage aqueous lithium-ion chemistries, Science 350 (6263) (2015) 938–943.

[36] J. Zheng, G. Tan, P. Shan, T. Liu, J. Hu, Y. Feng, L. Yang, M. Zhang, Z. Chen, Y. Lin, J. Lu, J.C. Neuefeind, Y. Ren, K. Amine, L.-W. Wang, K. Xu, F. Pan, Understanding thermodynamic and kinetic contributions in expanding the stability window of aqueous electrolytes, Chem 4 (12) (2018) 2872–2882.

[37] C.A.C. Ruiz, D. Bélanger, D. Rochefort, Electrochemical and spectroelectrochemical evidence of redox transitions involving protons in thin MnO_2 electrodes in protic ionic liquids, J. Phys. Chem. C 117 (40) (2013) 20397–20405.

[38] O. Munteshari, J. Lau, A. Krishnan, B. Dunn, L. Pilon, Isothermal calorimeter for measurements of time-dependent heat generation rate in individual supercapacitor electrodes, J. Power Sources 374 (2018) 257–268.

[39] O. Munteshari, J. Lau, D.S. Ashby, B. Dunn, L. Pilon, Effects of constituent materials on heat generation in individual EDLC electrodes, J. Electrochem. Soc. 165 (7) (2018) A1547–A1557.

[40] A. Likitchatchawankun, G. Whang, J. Lau, O. Munteshari, B. Dunn, L. Pilon, Effect of temperature on irreversible and reversible heat generation rates in ionic liquid-based electric double layer capacitors, Electrochim. Acta 338 (2020) 135802.

[41] A. Likitchatchawankun, R.H. DeBlock, G. Whang, O. Munteshari, M. Frajnkovič, B. Dunn, L. Pilon, Heat generation in electric double layer capacitors with neat and diluted ionic liquid electrolytes under large potential window between 5 and 80 °c, J. Power Sources 488 (2021).

[42] O. Munteshari, A. Borenstein, R.H. DeBlock, J. Lau, G. Whang, Y. Zhou, A. Likitchatchawankun, R.B. Kaner, B. Dunn, L. Pilon, In operando calorimetric measurements for activated carbon electrodes in ionic liquid electrolytes under large potential windows, ChemSusChem 13 (5) (2020) 1013–1026.

[43] L.H. Hess, A. Bothe, A. Balducci, Design and use of a novel in situ simultaneous thermal analysis cell for an accurate "real time" monitoring of the heat and weight changes occurring in electrochemical capacitors, Energy Technology 9 (9) (2021) 2100329.

[44] Y. Dandeville, P. Guillemet, Y. Scudeller, O. Crosnier, L. Athoul, T. Brousse, Measuring time-dependent heat profiles of aqueous electrochemical capacitors under cycling, Thermochim. Acta 526 (1–2) (2011) 1–8.

[45] C.-C. Ji, M.-W. Xu, S.-J. Bao, C.-J. Cai, R.-Y. Wang, D.-Z. Jia, Effect of alkaline and alkaline–earth cations on the supercapacitor performance of MnO_2 with various crystallographic structures, J. Solid State Electrochem. 17 (5) (2013) 1357–1368.

[46] J. Shin, J.K. Seo, R. Yaylian, A. Huang, Y.S. Meng, A review on mechanistic understanding of MnO_2 in aqueous electrolyte for electrical energy storage systems, Int. Mater. Rev. 65 (6) (2019) 356–387.

[47] S. Devaraj, N. Munichandraiah, Effect of crystallographic structure of MnO_2 on its electrochemical capacitance properties, J. Phys. Chem. C 112 (11) (2008) 4406–4417.

[48] A. Boisset, L. Athoul, J. Jacquemin, P. Porion, T. Brousse, M. Anouti, Comparative performances of birnessite and cryptomelane MnO_2 as electrode material in neutral aqueous lithium salt for supercapacitor application, J. Phys. Chem. C 117 (15) (2013) 7408–7422.

[49] A. Likitchatchawankun, A. Kundu, O. Munteshari, T.S. Fisher, L. Pilon, Heat generation in all-solid-state supercapacitors with graphene electrodes and gel electrolytes, Electrochim. Acta 303 (2019) 341–353.

[50] J. Schiffer, D. Linzen, D.U. Sauer, Heat generation in double layer capacitors, J. Power Sources 160 (1) (2006) 765–772.

[51] A.L. d'Entremont, L. Pilon, First-principles thermal modeling of electric double layer capacitors under constant-current cycling, J. Power Sources 246 (2014) 887–898.

[52] A. Hauch, S.D. Ebbesen, S.H. Jensen, M. Mogensen, Highly efficient high temperature electrolysis, J. Mater. Chem. 18 (20) (2008) 2331.

[53] C. Douard, L. Athoul, D. Brown, O. Crosnier, G. Rebmann, O. Schilling, T. Brousse, Electrode design for MnO_2-based aqueous electrochemical capacitors: Influence of porosity and mass loading, Materials 14 (11) (2021) 2990–3009.

[54] R.D. Shannon, Revised effective ionic radii and systematic studies of interatomic distances in halides and chalcogenides, Acta Crystallogr. Sect. A 32 (5) (1976) 751–767.

[55] J. Mähler, I. Persson, A study of the hydration of the alkali metal ions in aqueous solution, Inorg. Chem. 51 (1) (2011) 425–438.

[56] H. Wang, L. Pilon, Reply to comments on "intrinsic limitations of impedance measurements in determining electric double layer capacitances" by h. Wang, L. Pilon [electrochimica acta 63 (2012) 55], Electrochim. Acta 76 (2012) 529–531.

[57] A. Burke, M. Miller, Testing of electrochemical capacitors: Capacitance, resistance, energy density, and power capability, Electrochim. Acta 55 (25) (2010) 7538–7548.

[58] S. Zhao, F. Wu, L. Yang, L. Gao, A. Burke, A measurement method for determination of DC internal resistance of batteries and supercapacitors, Electrochem. Commun. 12 (2) (2010) 242–245.

[59] M.D. Stoller, R.S. Ruoff, Best practice methods for determining an electrode material's performance for ultracapacitors, Energy Environ. Sci. 3 (9) (2010) 1294–1301.

[60] B.-A. Mei, O. Munteshari, J. Lau, B. Dunn, L. Pilon, Physical interpretations of nyquist plots for EDLC electrodes and devices, J. Phys. Chem. C 122 (1) (2018) 194–206.

[61] Y. Marcus, Ionic radii in aqueous solutions, Chem. Rev. 88 (8) (1988) 1475–1498.

[62] A.M. Friedman, J.W. Kennedy, The self-diffusion coefficients of Potassium, Cesium, Iodide and Chloride ions in aqueous solutions, J. Am. Chem. Soc. 77 (17) (1955) 4499–4501.

[63] K. Tanaka, Measurements of tracer diffusion coefficients of sulphate ions in aqueous solutions of ammonium sulphate and sodium sulphate, and of water in aqueous sodium sulphate solutions, J. Chem. Soc. Faraday Trans. 1 84 (8) (1988) 2895–2897.

[64] D.W. Smith, Ionic hydration enthalpies, J. Chem. Educ. 54 (9) (1977) 540–542.

[65] Y. Cheng, H. Zhang, S. Lu, C.V. Varanasi, J. Liu, Flexible asymmetric supercapacitors with high energy and high power density in aqueous electrolytes, Nanoscale 5 (3) (2013) 1067–1073.

[66] S.M.H. Hashemi, P. Karnakov, P. Hadikhani, E. Chinello, S. Litvinov, C. Moser, P. Koumoutsakos, D. Psaltis, A versatile and membrane-less electrochemical reactor for the electrolysis of water and brine, Energy Environ. Sci. 12 (5) (2019) 1592–1604.

[67] H.-S. Kim, J.B. Cook, S.H. Tolbert, B. Dunn, The development of pseudocapacitive properties in nanosized-MoO_2, J. Electrochem. Soc. 162 (5) (2015) A5083–A5090.

[68] C.-H. Lai, D. Ashby, M. Moz, Y. Gogotsi, L. Pilon, B. Dunn, Designing pseudocapacitance for Nb_2O_5/carbide-derived carbon electrodes and hybrid devices, Langmuir 33 (37) (2017) 9407–9415.

[69] H. Wang, L. Pilon, Physical interpretation of cyclic voltammetry for measuring electric double layer capacitances, Electrochim. Acta 64 (2012) 130–139.

[70] A.L. d'Entremont, H.-L. Girard, H. Wang, L. Pilon, Electrochemical transport phenomena in hybrid pseudocapacitors under galvanostatic cycling, J. Electrochem. Soc. 163 (2) (2015) A229–A243.

[71] H. Dotan, A. Landman, S.W. Sheehan, K.D. Malviya, G.E. Shter, D.A. Grave, Z. Arzi, N. Yehudai, M. Halabi, N. Gal, N. Hadari, C. Cohen, A. Rothschild, G.S. Grader, Decoupled hydrogen and oxygen evolution by a two-step electrochemical–chemical cycle for efficient overall water splitting, Nat. Energy 4 (9) (2019) 786–795.

[72] J. Rumble, CRC Handbook of Chemistry and Physics, CRC Press/Taylor & Francis, Boca Raton, FL, 2020.

[73] A.L. d'Entremont, L. Pilon, First-principles thermal modeling of hybrid pseudocapacitors under galvanostatic cycling, J. Power Sources 335 (2016) 172–188.